



HAL
open science

Constitutive elasto-plastic model for fine soils in the unsaturated to saturated saturation zone

A. Fabbri, H. Wong, B Lai, T. Bui, D Branque

► **To cite this version:**

A. Fabbri, H. Wong, B Lai, T. Bui, D Branque. Constitutive elasto-plastic model for fine soils in the unsaturated to saturated saturation zone. *Computers and Geotechnics*, 2019, 10.1016/j.compgeo.2019.03.001 . hal-02389877

HAL Id: hal-02389877

<https://hal.science/hal-02389877>

Submitted on 2 Dec 2019

HAL is a multi-disciplinary open access archive for the deposit and dissemination of scientific research documents, whether they are published or not. The documents may come from teaching and research institutions in France or abroad, or from public or private research centers.

L'archive ouverte pluridisciplinaire **HAL**, est destinée au dépôt et à la diffusion de documents scientifiques de niveau recherche, publiés ou non, émanant des établissements d'enseignement et de recherche français ou étrangers, des laboratoires publics ou privés.

Constitutive elasto-plastic model for fine soils in the unsaturated to saturated saturation zone.

A. Fabbri^{a,*}, H.K.K. Wong^a, B. Lai^a, T.A. Bui^{a,b}, D. Branque^a

^a*LTDS, UMR 5513 CNRS, ENTPE, 2 rue Maurice Audin, 69100 Vaulx-en-Velin, France*

^b*Plaxis bv, Competence Centre Geo-Engineering, P.O. Box 572, 2600 AN Delft, The Netherlands*

Abstract

Near saturation, air bubbles and pockets can be trapped in the porous network of soils. The aim of this paper was to present a coupled model that takes into account the effect of this entrapped air on the poro-elasto-plastic behavior of the soil. The model takes into account the physical-mechanical interactions between different phases as well as the kinematics of each constituent (liquid water, dissolved air, gaseous air and solid grains). This new model was implemented in a FEM code. Some numerical simulations were performed to demonstrate its ability to reproduce a continuous transition of unsaturated to saturated states.

Keywords: Quasi-saturated soils; poro-elasto-plasticity; entrapped air in porous media

1. Introduction

For the design and the construction of geostructures, the knowledge of the response of soils subjected simultaneously to mechanical and hydraulic loadings is essential. In general, soils can be considered as multiphase porous media composed of the solid phase and porous space. Two or even more fluid phases can be simultaneously present in the porous space. For most cases in geotechnics, the two fluid phases are a liquid phase (water with other species) and a gas phase (air, water vapor). The hydromechanical behavior of soils depends not only on the constitutive behaviour of the solid skeleton, but also on the interaction between different phases.

Many experimental results have shown the important role of the gaseous phase in the hydromechanical behaviour of soils [1, 2, 3, 4]. And this effect was already taken into account in numerous constitutive elasto-plastic models [5, 6, 7, 8, 9].

*Corresponding author

Email addresses: antonin.fabbri@entpe.fr (A. Fabbri), kwaikwan.wong@entpe.fr (H.K.K. Wong), batien.lai@entpe.fr (B. Lai), t.bui@plaxis.com (T.A. Bui), denis.branque@entpe.fr (D. Branque)

Actually, at degrees of saturation lower than 85%, the gaseous phase is continuous. The coexistence of liquid water (a wetting liquid) and gaseous air (non-wetting gas) leads to the surface tension phenomenon, and a difference between their pressures, commonly called "suction". It results in an apparent attraction between grains, thus increasing the intergranular normal contact force. This has the effect of increasing the shear strength and the stiffness of the soil skeleton.

If a fair number of theoretical and experimental studies have explored the behavior of unsaturated soils, it is not the case for the transition between partially saturated and fully saturated states, called the "quasi-saturated state", which is almost never considered. The lack of researches in this domain is not in line with its importance. Indeed, earthwork materials are usually compacted to their optimum Proctor density. Under this condition, the saturation degree is close to 80% and the gaseous phase, which is no longer continuous, takes the form of air pockets and bubbles entrapped within the liquid phase [10]. The presence of this entrapped air seems to significantly influence the behavior of the soil. Several studies indicate that the entrapped air affects the soil's hydraulic and mechanical properties [11, 12, 13]. However, at the degree of saturation mentioned above, it appears that neither unsaturated nor saturated formalisms can accurately reproduce the behavior of fine compacted soils.

For that purpose, a first coupled hydro elastic model that takes into account the physical-mechanical interactions between different phases as well as the kinematics of each constituent (liquid water, dissolved air, gaseous air and solid grains) has been recently developed [14]. In particular, this model accounts for the interfacial tension, migration of gaseous and liquid phases, which have important impacts on the mechanical behaviour. The development leads to a system of highly non-linear partial differential equations which can be solved numerically using the finite element method. This model developed allows simulating the quasi-saturated soils behaviors and the continuous transition between the saturation domains. In order to complete the model presented in [14], the main objective of this paper is to present an extension of the theoretical developments to the elastoplastic behaviors of soils. At first, physical descriptions of air entrapment process in soil and air content evolution are presented. A simplification of the mass conservation equation, based on the analysis of characteristic time of the diffusion process of dissolved air is proposed. The second part of the paper is dedicated to the development of elasto-plastic law of behavior. For that purpose, a definition of the generalized effective stress for all saturation domains is introduced, as well as some assumptions on the evolution of loading surface with suction in the quasi-saturated domain. At last, the new model has been implemented in a numerical code Hydromech written in C++, developed originally by [15], that has been used to simulate oedometer tests with different hydromechanical loading paths.

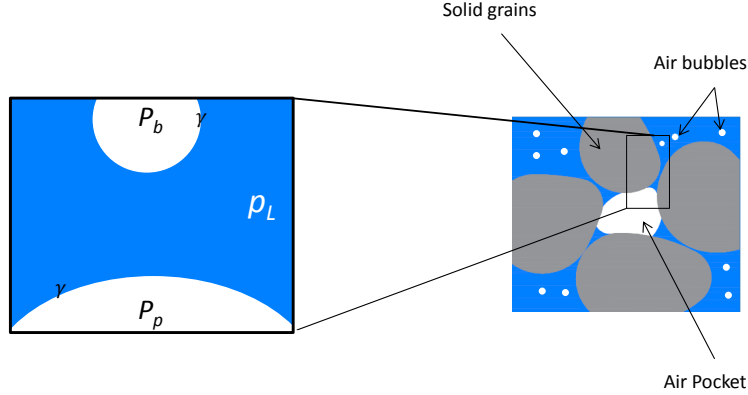


Figure 1: Schematic representation of the entrapped air pockets and air bubbles within the porous network

2. Description of entrapped air

2.1. Air bubbles and air pockets

The air phase is defined as "entrapped" when it is no longer in contact with the external atmosphere. As already discussed by Vaughan [16], for a given entrapped air volume, all the air molecules can either be formulated as numerous spherical bubbles of radius r_{bubble} embedded within the liquid phase or take a more complex geometry that closely follows the shape of the porous space to maximize its volume-to-surface ratio. A schematic diagram of the distinction between air bubbles and air pockets is reported in Figure 1.

The migration of air bubbles through the porous network can be due to their advection by the liquid phase or by their transport within the liquid phase, which can be regarded as a diffusion process. At constant pressure and temperature, they do not modify the free energy of the solid matrix. Their sole mechanical impact is to reduce the apparent compressibility of the liquid phase. The absence of interaction with the surface of the pores forces these bubbles to have a radius lower than the characteristic percolation size of the porous network, denoted by r_{perc} . If not, their unobstructed movement across the porous space network becomes unlikely and the spherical geometry of the entrapped air volumes may be modified at their interactions with the surface of the pores. In this case, the entrapped air is assumed to form air pockets whose spatial migration can only take place by dissolution in liquid water followed by advective transport and Fickian diffusion of the dissolved air molecules (see, for example, [17]). Due to evident geometrical constraints, the radius of the liquid-gas interface, r_{pocket} , is lower than the radius of the pore, r_p where the pocket is located. This description gives the following relation between the radii of the porous network and of the liquid-gas interfaces:

$$r_{\text{bubble}} < r_{\text{perc}} \leq r_{\text{pocket}} \leq r_p. \quad (1)$$

2.2. Equilibrium between gaseous and dissolved air molecules

The thermodynamic equilibrium between dissolved air and gaseous air is assumed to be reached anywhere at any time. Consequently, at constant pressure, the air pocket dissolution kinetics are driven by the velocity of dissolved air-molecule migration within the liquid phase, while the dissolution/bubbling processes induced by gas pressure variation are assumed to be instantaneous. Under the assumption of dilute solutions and perfect gas, the amount of air dissolved in liquid water is directly linked to the gaseous air pressure through Henry's law (cf. [14] for more details):

$$P_G = K_H \frac{M_{\text{H}_2\text{O}}}{M_G} \bar{m}^{eq}, \quad (2)$$

where P_G is the gas pressure, \bar{m}^{eq} is the mass of dissolved air per unit of liquid water mass at equilibrium with the entrapped air pockets, $M_{\text{H}_2\text{O}}$ and M_G are the molar mass of water and air, respectively, and K_H is Henry's constant. At 20°C, and assuming that air is composed of 20% O₂ and 80% N₂, $K_H \approx 7300$ MPa.

The use of the Henry's law requires the existence of stable air pockets within the pore network of the REV. To account for the full saturation case, we introduce \bar{m} , which is the mass of dissolved air per unit of liquid water mass:

$$\bar{m} = \frac{m_{\text{aL}}}{m_L}, \quad (3)$$

where m_{aL} is the mass of dissolved air per unit of total initial volume (that is volume of solid matrix and pore space) and m_L is the mass of liquid water per unit of total initial volume.

When the air in the gaseous state still exists within the REV, $S_L < 1$, we have $\bar{m} = \bar{m}^{eq}$. When the fully saturated state is reached $S_L = 1$ (that is when all the pore air in the REV has been dissolved), eq. (2) is no longer applicable. In this case, $\bar{m} \leq \bar{m}^{eq}$. In this case the following conditions are considered:

$$\bar{m}^{eq} \geq \bar{m} \geq 0 ; 1 \geq S_L \geq 0 ; (\bar{m} - \bar{m}^{eq})(1 - S_L) = 0. \quad (4)$$

The relation (2) indicates that the dissolution process is directly related to the gas pressure within the air pockets, which is in turn linked to the shape of the liquid-air interface through Young-Laplace's law:

$$P_G - P_L = \frac{2\gamma_{\text{L,G}}}{r}, \quad (5)$$

where P_L is the liquid pressure, $\gamma_{\text{L,G}}$ is the surface tension of the liquid-gas interface, r is its radius, which is assumed to be spherical, $r = r_{\text{bubble}}$ for the air bubbles and $r = r_{\text{pocket}}$ for the air pockets. Since $r_{\text{bubble}} < r_{\text{pocket}}$, the

combined use of eqs. (2) and (5) results in a higher concentration of dissolved air in the vicinity of the air bubbles than in the vicinity of the air pockets. As a consequence, dissolved air migrates from the bubbles toward the pockets, which ultimately makes the bubbles disappear in favor of the pockets. Because the characteristic diffusion time at the pore scale is much shorter than other characteristic times at the structural scale, the coalescence of small air pockets is assumed to be instantaneous.

In conclusion to this analysis, trapped air is assumed to take exclusively the form of air pockets (spherical or non-spherical) whose kinematics are similar to the solid skeleton's. To assess the geometry of these pockets, and especially of their interface with the surrounding liquid phase, it is necessary to make assumptions on how these pockets are created and their evolution.

2.3. From partial saturation to saturation: air entrapment mechanism

The physical origin of air entrapment can be explained by the diagram in Figure 2A: during wetting of an initially partially saturated soil, the smaller pores of the porous network are invaded by the liquid phase, which forces the evacuation of the gaseous phase out of the medium through the connected network of larger pores, which remain dried [18]. When the saturation ratio increases above a certain threshold, denoted by S_e^E , which is close to 90% (cf. [18], for example), all the pores with a radius lower than or equal to the percolation radius become saturated by water. At that stage, the gas's relative permeability reaches zero, but some air remains in the larger pores. This air can be considered as "entrapped" since all the capillaries that connect these pores to the rest of the porous network are saturated with water. The total volume of entrapped air within an REV with an initial volume of $d\Omega^0$ just after connectivity of the gas phase is lost is equal to $\phi(1 - S_e^E)d\Omega^0$, where ϕ is the Lagrangian porosity. It should be remembered that the capillary pressure, or suction, is defined as the difference between the nonwetting fluid (G) and the wetting fluid (L): $P_c = P_G - P_L$. The value of P_c needed to reach saturation S_e^E is denoted by $P_{c,e}$ and, assuming a spherical liquid-gas interface, a negligible thickness of the water adsorbed layer, and a wetting angle of 0° , is equal to:

$$P_{c,e} = \frac{2\gamma_{L,G}}{r_{\text{perc}}}. \quad (6)$$

Rigorously, $P_{c,e}$ should be called "percolation suction" since it marks the transition between a continuous and a discontinuous gas phase. For the sake of simplicity, we assume here that $P_{c,e}$ can be confounded with entry air suction, which means that the hysteresis between drainage and wetting is ignored.

According to this description, the interface radius of all the air pockets just after their creation during a wetting process is equal to r_{perc} . After this stage, the geometry of the pockets may change due to dissolution/bubbling processes or to their mechanical deformation. Whatever these transformations, they take on a shape that maximizes their interface radius with the surrounding liquid phase. It is quite difficult to predict the evolution of the optimal interface radius with

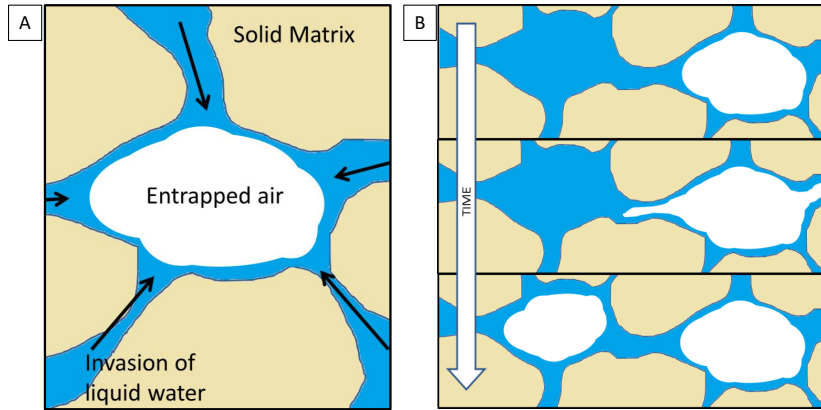


Figure 2: A: Schematic representation of the air entrapment process. B: Diagram of the snap-off effect.

air content since the geometry of the air pocket may be quite complex. To overcome this problem, any decrease of air content is assumed to induce a reduction of the number of pockets rather than the decrease of their size; and vice-versa, the air content increase leads to the creation of new air pockets of optimized size, which may be notably induced by the so-called snap-off effect (see Figure 2B). This assumption seems to be in agreement with the microtomography observations made by [19]. It may be explained by the fact that the volume and the shape of air pockets are driven by the geometry of the pore where they are trapped. At equilibrium, the trapped air phase consists of numerous pockets with the same liquid-gas interface radii, which are as high as possible. When the air content decreases, some pockets may be more impacted by others. These pockets will then dissolve and feed the other (more stable) pockets so that they keep the same geometry.

In conclusion, all the stable pockets are assumed to have the same interface radius with the liquid phase, and this radius is assumed to remain constant and equal to r_{perc} . A consequence of this assumption is that, even if the entrapped air is in the form of isolated pockets, its pressure is homogeneous within a RVE and the poromechanical mixture theory's approach, notably presented in [20], can be applied.

2.4. From saturation to partial saturation: air entrance mechanism

Creation of embedded air pockets and bubbles within the liquid phase during a drainage stage from the fully saturated state can result from two major mechanisms. The first one is the heterogeneous nucleation of dissolved air. However, a rough estimation using a formalism similar to the one presented in [21] leads to the occurrence of nucleation for a supersaturation of dissolved air within the range of 1.1-1.2, which is quite unlikely in geotechnical applications.

The second mechanism is the *snap-off* effect. However, this effect remains located near the external surfaces of the material and should occur for suction levels within the range of entry air suction.

In conclusion, a direct transition, without the occurrence of trapped air, is assumed from the saturated to the unsaturated domains.

2.5. Conclusions on the definition of in-pore phases and the limits of saturation domains

For the sake of simplicity, the gravity term is not considered in the following development.

The above physical description leads to the consideration of two in-pore phases (liquid, L, and gas, G), each composed of two components: the liquid phase is made of liquid water (w) and dissolved air (aL), while the gas phase is made of dry air (aG) and water vapor (v). In addition, two types of distinct behavior have been identified for the gas phase: it can be either free if $P_{\text{atm}} - P_L \geq P_{c,e}$ or trapped if $P_{\text{atm}} - P_L < P_{c,e}$. To facilitate the integration of this discontinuity into the equations, without loss of generality, the gaseous phase will conceptually be divided into two sets that can freely exchange within each other (see Figure 3). The first is the part that is invaded by water during the wetting process before the loss of connectivity of the gaseous phase. The gaseous phase within this volume is denoted with the superscript (m). The remaining part therefore corresponds to locations where the air is entrapped when the saturation attains the threshold S_e . The air within this volume is denoted by the superscript (t). It is important to underline that this distinction between these two geometrical domains of the air phase is only made to simplify the derivations and that it is not necessary for the development of the model. Using these notations, the saturation ratio can be expressed as:

$$S_L = 1 - S_{\text{aG}}^{(m)} - S_{\text{aG}}^{(t)}, \quad (7)$$

where S_L is the saturation ratio, $S_{\text{aG}}^{(m)}$ is the fraction of the volume presently occupied by the gaseous phase that is invaded by the liquid phase when $S_L = S_e$ (or when $P_{\text{atm}} - P_L = P_{c,e}$), while $S_{\text{aG}}^{(t)}$ represents the complementary part that remains to be occupied by the entrapped air when $S_L = S_e$ (or when $P_{\text{atm}} - P_L = P_{c,e}$).

The porous medium is considered "unsaturated" as long as the gaseous phase remains continuous and connected. This happens when the difference between the atmospheric pressure and the in-pore liquid pressure is higher than the entry air suction. Within this domain, the relationship between suction and saturation degree is depicted by the retention curve. A fairly large number of closed-form equations exist to reproduce this curve accurately for different materials. In this study we use the prominent equation provided by Brooks and Corey [22] for saturation ratios ranging between 0 and S_e :

$$S_L = S_e \left(\frac{P_{\text{atm}} - P_L}{P_{c,e}} \right)^{-a} \quad \text{for } P_{\text{atm}} - P_L \geq P_{c,e}. \quad (8)$$

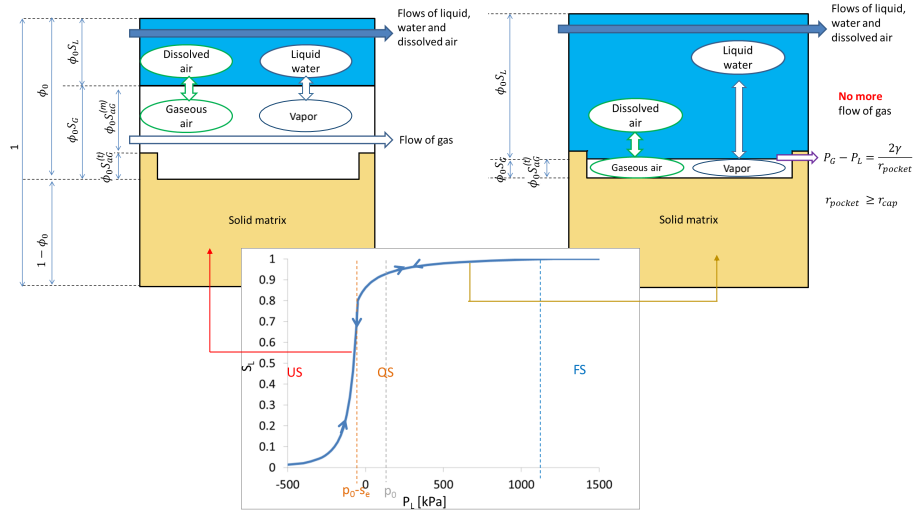


Figure 3: Shape of the retention curve and diagram of the unsaturated and quasi-saturated domains

The combination of (7) and (8) gives:

$$S_{aG}^{(m)} = S_e \left(1 - \left(\frac{P_{atm} - P_L}{P_{c,e}} \right)^{-a} \right) \text{ for } P_{atm} - P_L \geq P_{c,e}, \quad (9a)$$

$$S_{aG}^{(t)} = 1 - S_e \text{ for } P_{atm} - P_L \geq P_{c,e}. \quad (9b)$$

When the gaseous phase becomes discontinuous (no "free" air is left), $S_{aG}^{(m)}$ becomes null and the gas pressure can exceed P_{atm} . According to the description of air pockets presented above, and assuming that $p_v \ll p_{aG}$, the link between the gas pressure and the liquid pressure is:

$$P_G = P_L + P_{c,e} \approx p_{aG} \text{ for } P_{atm} - P_L \leq P_{c,e}, \quad (10)$$

where p_{aG} is the partial pressure of dry air.

The quantity of entrapped air can change due to dissolution or bubbling. When all of the entrapped air is dissolved, the material becomes fully saturated. The mathematical conditions that define the fully saturated states are $S_{aG} = 0$ and $P_{atm} - P_L \leq P_{c,e}$. This description leads to the shape of the retention curve shown in Figure 3.

The impact of the compaction on the transition between the unsaturated and the quasi-saturated domains is taken into account through the variation of $P_{c,e}$ with the void ratio. The general tendency, which is observed on alluvial soils by [23], and on finer soils by [24], is a decrease of $P_{c,e}$ when the void ratio

increase. But this relation is not unique and must be experimentally determined for each soil.

3. Behavior of the in-pore phases

3.1. Mass conservation equations

To predict the behavior of both liquid and gas phases, it is necessary to consider two distinct mass conservations equations. In this paper, similarly to what is done in [14], the mass conservations of water (both liquid and vapour) and air (both gaseous and dissolved) are chosen. It leads to the following system of equation (For more detail, see [14]):

$$\frac{\rho_L^0 e}{1 + e_0} \left(A_e \frac{\partial e}{\partial t} + A_p \frac{\partial P_L}{\partial t} - \frac{\partial S_{aG}^{(t)}}{\partial t} \right) = \nabla \cdot (D_L \nabla P_L), \quad (11)$$

$$\begin{aligned} \frac{\rho_L^0 e}{1 + e_0} \left(S_L \frac{\partial \bar{m}}{\partial t} + B_p \frac{\partial P_L}{\partial t} + B_e \frac{\partial e}{\partial t} + \left(\beta_1 \frac{\rho_G}{\rho_L^0} - \bar{m} \right) \frac{\partial S_{aG}^{(t)}}{\partial t} \right) \\ = \nabla \cdot (\bar{m} D_L \nabla P_L + \rho_L D_e \nabla \bar{m}), \quad (12) \end{aligned}$$

with

$$\begin{aligned} A_p &= \frac{S_L}{K_L} - \frac{\partial S_{aG}^{(m)}}{\partial P_L} \\ A_e &= \frac{S_L}{e} - \frac{\partial S_{aG}^{(m)}}{\partial e} \\ B_p &= \bar{m} \left(\frac{S_L}{K_L} - \frac{\partial S_{aG}^{(m)}}{\partial P_L} \right) + \beta_1 \frac{\rho_G}{\rho_L^0} \frac{S_{aG}^{(t)}}{P_G} \\ B_e &= \bar{m} \left(\frac{S_L}{e} - \frac{\partial S_{aG}^{(m)}}{\partial e} \right) + \beta_1 S_{aG}^{(t)} \frac{\rho_G}{\rho_L^0} \left(\frac{1}{e} + \frac{1}{P_G} \frac{\partial P_{c,e}}{\partial e} \right), \end{aligned}$$

where, ρ_L is the density of liquid water, K_L its bulk modulus, ρ_G is the density of the gas, e is the void ratio and e_0 is the initial void ratio. $\partial S_{aG}^{(m)}/\partial e$ and $\partial S_{aG}^{(m)}/\partial P_L$ can be calculated in accordance with the relation (9). D_e is the effective diffusion coefficient of dissolved air within the liquid water and D_L is the global permeability coefficient of water, which is equal to:

$$D_L = \left(\mathcal{K}_L + \frac{c_v}{\rho_L} \delta_p \right), \quad (13)$$

with c_v the mass concentration of vapor per unit of gas volume, \mathcal{K}_L the transport coefficient of liquid water, and δ_p the transport coefficient of vapor. They satisfy:

$$\mathcal{K}_L = \rho_L^0 \frac{\kappa_0 \kappa_r^L}{\eta_L}; \quad \delta_p = D_e^v \frac{M_{H_2O}}{RT}, \quad (14)$$

where κ_0 is the material's intrinsic permeability, in m^2 ; κ_r^L is liquid water's relative permeability coefficient, which is a nondimensional quantity that varies between 0 (at a low saturation ratio) and 1 (when the material is fully saturated); η_L is the dynamic viscosity of liquid water; D_e^v is the effective diffusion coefficient of water vapor within the air phase, R is the perfect gas constant, T the absolute temperature and $M_{\text{H}_2\text{O}}$ the molar mass of water.

For the variation of \mathcal{K}_L with saturation, the relation proposed by Martin et al. [25] is used, due to its simplicity and its quite good consistency with experimental data on fine soils:

$$\mathcal{K}_L = \mathcal{K}_L^0 (S_L)^3, \quad (15)$$

where $\mathcal{K}_L^0 = \rho_L^0 \kappa_0 / \eta_L$ is the value of \mathcal{K}_L at full saturation.

For the variation of δ_p , Millington's expression [26] is arbitrarily chosen:

$$\delta_p = \delta_p^0 (1 - S_L)^{7/3}, \quad (16)$$

where δ_p^0 is the value of δ_p for a dried material.

Finally, β_1 is defined by:

$$\beta_1 = \mathcal{Y}(P_{c,e} - P_{\text{atm}} + P_L), \quad (17)$$

with $\mathcal{Y}(x) = 0$ for $x < 0$ and $\mathcal{Y}(x) = 1$ otherwise (step function). In other words, $\beta_1 = 0$ for the unsaturated domain and $\beta_1 = 1$ for the quasi-saturated and fully saturated domains.

The final step to close the system is to consider the equilibrium between gaseous and dissolved air, as is depicted by the relation (4). In other words, \bar{m} should be equal to $\bar{m}^{eq} = (P_G M_G) / (M_{\text{H}_2\text{O}} K_H)$ in the unsaturated and quasi-saturated domains, while $S_{\text{aG}}^{(t)} = 0$ in the fully saturated domain. A necessary and sufficient condition to fulfill these two conditions is to consider the following form for the variation of $S_{\text{aG}}^{(t)}$:

$$\frac{\partial S_{\text{aG}}^{(t)}}{\partial t} = \beta_2 \left(C_p \frac{\partial P_L}{\partial t} + C_e \frac{\partial e}{\partial t} - \nabla \cdot \left(\bar{m} \left(\mathcal{K}_L + \frac{c_v}{\rho_L} \delta_p \right) \nabla P_L + \rho_L D_e \nabla \bar{m} \right) \right), \quad (18)$$

where

$$\begin{aligned} C_p &= \frac{\rho_L^0 e}{1 + e_0} \left(\bar{m}^{eq} \left(\frac{S_L}{K_L} - \frac{\partial S_{\text{aG}}^{(m)}}{\partial P_L} \right) + \frac{\beta_1}{P_G} \left(\bar{m}^{eq} S_L + \frac{\rho_G}{\rho_L^0} S_{\text{aG}}^{(t)} \right) \right) \\ C_e &= \frac{\rho_L^0 e}{1 + e_0} \left(\left(\bar{m}^{eq} S_L + \beta_1 S_{\text{aG}}^{(t)} \frac{\rho_G}{\rho_L^0} \right) \left(\frac{1}{e} - \beta_1 \frac{1}{P_G} \frac{\partial P_{c,e}}{\partial e} \right) - \bar{m}^{eq} \frac{\partial S_{\text{aG}}^{(m)}}{\partial e} \right) \end{aligned}$$

and

$$\beta_2 = \frac{(1 + e_0) \text{sign}(S_{\text{aG}})}{e\rho_{\text{L}}^0 \left(\bar{m}^{eq} - \beta_1 \frac{\rho_{\text{G}}}{\rho_{\text{L}}} \right)}, \quad (19)$$

with $\text{sign}(S_{\text{aG}})=0$ when $S_{\text{aG}} = 0$ (when the material is fully saturated) and $\text{sign}(S_{\text{aG}})=1$ when $S_{\text{aG}} > 0$ (the material is either unsaturated or quasi-saturated).

3.2. Simplification of the system of equation

The analysis of the relations (12) and (18) leads to the definition of τ_D , which is the characteristic time of the dissolved air diffusion:

$$\tau_D \approx \frac{e}{1 + e_0} \frac{L^2}{D_e^v}, \quad (20)$$

where L is the characteristic length.

If τ_D is strongly higher than the characteristic time of the solicitation and/or observation, the diffusion processes can be ignored, and the system of equation (11), (12), and (18) is simplified to:

$$\frac{\rho_{\text{L}}^0 e}{1 + e_0} \left(A_e \frac{\partial e}{\partial t} + A_p \frac{\partial P_{\text{L}}}{\partial t} - \frac{\partial S_{\text{aG}}^{(t)}}{\partial t} \right) = \nabla \cdot (D_{\text{L}} \nabla P_{\text{L}}), \quad (21a)$$

$$\frac{\partial S_{\text{aG}}^{(t)}}{\partial t} = \beta_2 \left(C_p \frac{\partial P_{\text{L}}}{\partial t} + C_e \frac{\partial e}{\partial t} - \nabla \cdot (\bar{m}^{eq} D_{\text{L}} \nabla P_{\text{L}}) \right). \quad (21b)$$

3.3. Numerical application of the mass conservation equations

To illustrate the system formed by equations (11), (12), and (18), a first calculation was performed considering an undeformable porous material (i.e., for $\partial e/\partial t = 0$). This calculation considered the 1D configuration of a cylindrical 5-cm-high sample totally isolated on its lateral surfaces. This was done using the data reported in Table 1 and the calculation was performed with a home-made finite volume code computed in C.

The sample was initially in the unsaturated domain, with a saturation ratio equal to $S_{\text{L}}^0 = 0.0012$ and therefore:

$$P_{\text{L}}(x, t = 0) = P_0 = P_{\text{atm}} - P_{c,e} \left(\frac{S_e}{S_{\text{L}}^0} \right)^{(1/a)} = 10 \text{kPa} \quad (22a)$$

$$\bar{m}(x, t = 0) = \bar{m}_0 = \frac{M_{\text{G}} P_{\text{atm}}}{K_{\text{H}} M_{\text{H}_2\text{O}}} = 2.2 \times 10^{-5} \quad (22b)$$

$$S_{\text{aG}}^{(t)}(x, t = 0) = 1 - S_e \quad (22c)$$

At $t = 0$ the material was put in contact with liquid water at one end of the sample. Its pressure linearly increased from $P_0 = 10$ [kPa] to P_{atm} in 864 s and remained constant until the end of the simulation. The dissolved air content

Symbol	Description	Value [unity]
T	Temperature	293 [K]
P_{atm}	Atmospheric pressure	100 [kPa]
K_H	Henry's constant	7326 [MPa]
R	Perfect gas constant	8.314 [J/K/mol]
K_L	Bulk modulus of liquid water	1970 [MPa]
$M_{\text{H}_2\text{O}}$	Molar mass of water	18 [g/mol]
ρ_L	Density of water	1000 [kg/m ³]
M_G	Molar mass of air	29 [g/mol]
e_0	Void ratio	0.53
S_e	Degree of saturation at air entry	0.9
$P_{c,e}$	Entry air suction	10 [kPa]
a	Coef. of the retention curve	3
D_e	Diffusion coef. of dissolved air	$2.2 \cdot 10^{-11}$ [m ² /s]
\mathcal{K}_L	transport coef. of liquid water	$1.43 \cdot 10^{-8}$ [s]
δ_p	Diffusion coef. of vapor	$1.5 \cdot 10^{-11}$ [s]

Table 1: Numerical values used for the simulation.

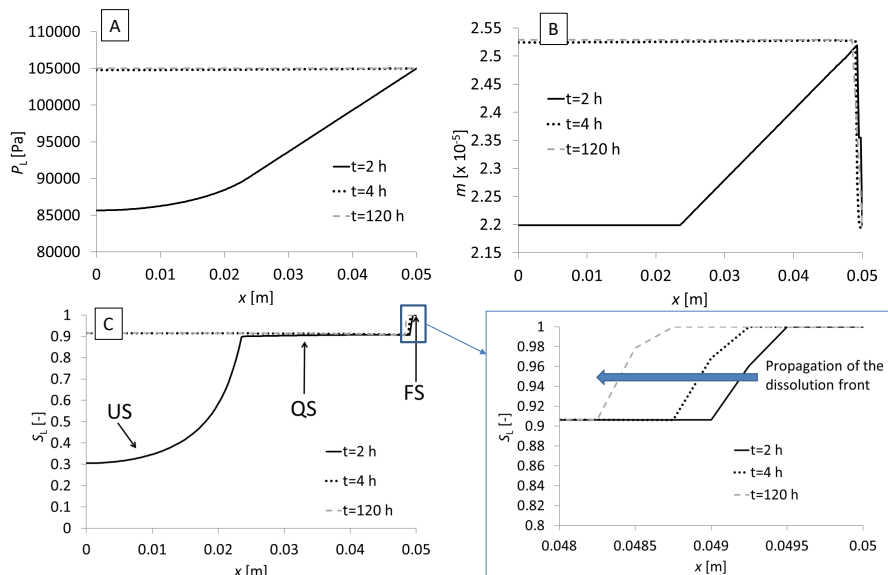


Figure 4: Liquid pressure (A), dissolved air content (B), and saturation ratio (C) profiles at three times obtained from the numerical application of the mass conservation equations for an undeformable porous medium.

within this water remained constant and equal to $\bar{m}_0 = 2.2 \times 10^{-5}$. The results of the simulation are reported in Figure 4.

At first the model shows spatial and temporal transitions from unsaturated domain to quasi-saturated domain. As long as $P_L < P_{\text{atm}} - P_{c,e} = 90$ [kPa],

the material is under the unsaturated domain. The evolution of the saturation ratio is driven by the relation (8), and \bar{m} remains constant and equal to \bar{m}_0 . When the material becomes quasi-saturated, the shape of the saturation ratio evolution changes and it is driven by the compressibility and dissolution of the air phase. The pressure of the gas phase is no longer equal to P_{atm} , which then increases the dissolved air content. As a result, a gradient of dissolved air content is created between the core of the material and its boundary, which will progressively dissolve all the entrapped air. The propagation of this dissolution front, which is driven by the diffusion process of dissolved air, is very slow (less than 2 mm in 150 h). This numerical example thus clearly shows that even though the diffusion of dissolved air must be taken into account to properly model the long term behavior of quasi-saturated soils, the simplified system of equation (12) and (18) may be acceptable when short term behavior is assessed.

4. Mechanical equilibrium and rheological law

4.1. Sign convention and definition of the mechanical variables

Most of the elasto-plastic laws for unsaturated soils were developed with the sign convention of soil mechanics. Consequently, in this paper compressive stresses are taken as positives and positive strains express contraction. To derive the rheological law, the classical scalar variables of the Cam Clay model, namely the volumetric strain ϵ_v , the mean stress σ_v , the deviatoric strain ϵ_d and the deviatoric stress σ_d , are used. They are linked to the stress and strain tensors through the relations:

$$\epsilon_v = \text{tr}(\boldsymbol{\epsilon}) ; \epsilon_d = \sqrt{\frac{2}{3} \boldsymbol{\epsilon}_d : \boldsymbol{\epsilon}_d}, \quad (23a)$$

$$\sigma_v = \frac{1}{3} \text{tr}(\boldsymbol{\sigma}) ; \sigma_d = \sqrt{\frac{3}{2} \boldsymbol{\sigma}_d : \boldsymbol{\sigma}_d}, \quad (23b)$$

where $\boldsymbol{\epsilon}$ and $\boldsymbol{\sigma}$ are the strain and stress tensors while $\boldsymbol{\epsilon}_d$ and $\boldsymbol{\sigma}_d$ are their deviatoric parts, which are defined by:

$$\boldsymbol{\epsilon}_d = \boldsymbol{\epsilon} - \frac{\epsilon_v}{3} \boldsymbol{\delta} ; \boldsymbol{\sigma}_d = \boldsymbol{\sigma} - \sigma_v \boldsymbol{\delta}, \quad (23c)$$

where $\boldsymbol{\delta}$ is the second order identity tensor.

For an axisymmetric problem, the relations (23) simplified in the form:

$$\epsilon_v = \epsilon_1 + 2\epsilon_2 ; \epsilon_d = \frac{2}{3} |\epsilon_1 - \epsilon_2|, \quad (24a)$$

$$\sigma_v = \frac{1}{3} (\sigma_1 + 2\sigma_2) ; \sigma_d = |\sigma_1 - \sigma_2|, \quad (24b)$$

where ϵ_1 and σ_1 are the principal strain and the principal stress along the axis of symmetry, while ϵ_2 and σ_2 are the principal stress and principal strain along

the radial and orthoradial directions.

Consistently with the classical strain decomposition assumption, volumetric and deviatoric strains can be split in elastic (superscript e) and plastic (superscript p) parts:

$$\epsilon_v = \epsilon_v^e + \epsilon_v^p ; \epsilon_d = \epsilon_d^e + \epsilon_d^p. \quad (25)$$

Under the soil mechanics sign convention the relation between the effective stress and the total stress is:

$$\boldsymbol{\sigma}' = \boldsymbol{\sigma} - \bar{P}_\phi \boldsymbol{\delta} ; \sigma'_v = \frac{1}{3}(\sigma_1 + 2\sigma_2) - \bar{P}_\phi, \quad (26)$$

where $\boldsymbol{\sigma}'$ is the effective stress tensor, σ'_v is the mean effective stress, \bar{P}_ϕ is the equivalent pore pressure. In the saturated regime, $\bar{P}_\phi = P_L$, and $\boldsymbol{\sigma}'$ is equal to Terzaghi's effective stress. In the quasi-saturated and unsaturated regime, the effect of the interfacial energy is ignored, $\bar{P}_\phi = (1 - \chi(S_L))P_G + \chi(S_L)P_L$, and $\boldsymbol{\sigma}'$ is equal to Bishop's effective stress. Finally, since this study focuses on the high saturation ratio, the assumption $\chi(S_L) = S_L$ is used. On the basis of these restrictions, the extensive use of the relation (17) that define the coefficient β_1 as well as the ones that specify the values of $S_{aG}^{(t)}$, $S_{aG}^{(m)}$ and P_G for the different domain of saturation (equations 7-10) and below), allows to write \bar{P}_ϕ and its temporal derivation in the forms:

$$\bar{P}_\phi = (\beta_1 + (1 - \beta_1)S_L)P_L + (1 - \beta_1)(1 - S_L)P_{atm} + \beta_1 S_{aG}^{(t)} P_{c,e}, \quad (27)$$

$$\frac{\partial \bar{P}_\phi}{\partial t} = [\beta_1 + (1 - \beta_1)(1 - a)S_L] \frac{\partial P_L}{\partial t} + P_{c,e} \frac{\partial S_{aG}^{(t)}}{\partial t}, \quad (28)$$

where we recall that a is the coefficient of the Brooks and Correy retention curve.

4.2. Elastoplastic rheological law

To describe the elastic behavior, the isotropic logarithmic elastic behavior of the Cam Clay model is adopted:

$$d\epsilon_v = \frac{d\sigma'_v}{K} ; K = \frac{1 + e_0}{\mathbf{k}} \sigma'_v, \quad (29a)$$

$$d\epsilon_d = \frac{d\sigma_d}{3G} ; G = \frac{3(1 - 2\nu)}{2(1 + \nu)} K, \quad (29b)$$

where e_0 denotes the initial void ratio, K and G are the bulk and the shear moduli, while ν , which is assumed to be constant, is the Poisson ratio. This elastic law leads to a linear variation of the volumetric strain (or void ratio)

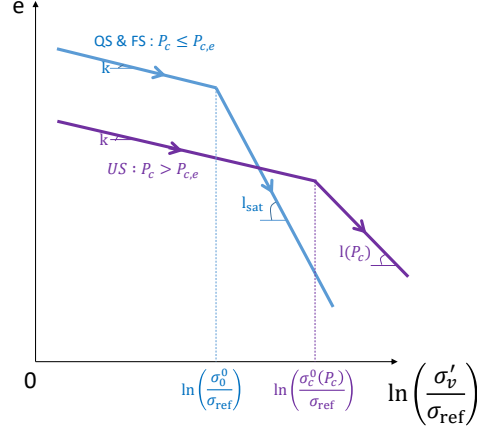


Figure 5: Variation of the void ratio with the logarithm of the mean effective stress during isotropic compressions at several suction values. σ_0^0 and σ_c^0 stand for the initial saturated and unsaturated preconsolidation stresses, respectively.

with the logarithm of the mean effective stress during an elastic isotropic compression, and the slope of this variation is equal to k (cf. Figure 5).

To describe the plastic behavior, the general framework of isotropic strain-hardening poroelastoplasticity (cf. [27]) is used with the following expression for the loading surface:

$$f(\sigma'_v, \sigma_d, \sigma_c) = \sigma_d^2 - M^2 \sigma'_v (\sigma_c - \sigma'_v). \quad (30)$$

In plane (σ'_v, σ_d) , it leads to the elliptic criterion drawn in the Figure (6A). The size of the loading surface is driven by a constant M , which is the slope of the critical state line, and the hardening dual variable σ_c . From a physical point of view, σ_c is the preconsolidation stress. That is, during an isotropic compression load, no plastic strain occurs as long as σ'_v remains strictly lower than σ_c . As a consequence, in the plane (σ'_v, P_c) , the variation of σ_c , which is described by the loading collapse curve (cf. Figure 6B), directly limits the elastic zone. Within the wide range of formulations available, a slight modification of Alonso et al.'s formulation [5] is chosen to describe the variation of σ_c with P_c :

$$\frac{\sigma_c}{\sigma_{\text{ref}}} = \left(\frac{\sigma_0}{\sigma_{\text{ref}}} \right)^{\frac{1_{\text{sat}} - k}{1(P_c) - k}}. \quad (31)$$

In this expression, σ_0 is the value of σ_c at full saturation. 1_{sat} is the stiffness parameter of saturated soil that corresponds to the slope of the void ratio variation with the logarithm of the effective mean stress during an isotropic virgin

compression (i.e., for σ'_v which is higher than the initial preconsolidation stress denoted by σ_c^0 in the Figure 5, and hence $\sigma_c = \sigma'_v$). The $\mathbf{1}(P_c)$ function in (31) accounts for the increase of resistance and stiffness with suction. The choice of this function's formulation is particularly important because it determines the shape of the loading surface, which then affects the capacity of the model to reproduce wetting collapse. When the material is quasi-saturated, on the basis of experimental studies on lateritic and saprolitic soils [28] as well as Gangetic silt and Canyon Dam clay [29], $\mathbf{1}(P_c)$ is assumed to remain equal to $\mathbf{1}_{\text{sat}}$. According to the relation (31), this assumption leads to $\sigma_c = \sigma_0$ when $P_c \leq P_{c,e}$. Despite the high number of experimental studies conducted on this subject, no clear tendencies have been observed when the material is unsaturated. In some studies, $\mathbf{1}$ increases P_c , while in others it decreases [8]. In this paper, to be consistent with the relation (31), a form similar to the one proposed by Alonso et al. [5] is adopted. It follows that the formulation of $\mathbf{1}(P_c)$ for the three domains of saturation can be described by:

$$\mathbf{1}(P_c) = (1 - \beta_1)\mathbf{1}_{\text{sat}} \left((1 - r) e^{-b(P_c - P_{c,e})} + r \right) + \beta_1\mathbf{1}_{\text{sat}}, \quad (32)$$

where b and r are two material parameters and β_1 is defined by the relation (17).

A direct consequence of this form of $\mathbf{1}(P_c)$ is that σ_c is equal to σ_0 in the quasi-saturated regime (cf. Figure 6). The physical meaning of this result is that no capillary hardening (or softening) is assumed as long as the air phase is entrapped, thus, from the point of view of the solid skeleton, the soil is saturated. Even if this result seems quite natural, it still needs to be experimentally verified.

Finally, the evolution of the preconsolidation pressure with the hardening variable, namely ϵ_v^p , is assumed to follow the Cam Clay incremental law:

$$d\sigma_0 = \frac{1 + e_0}{\mathbf{1}_{\text{sat}} - k} \sigma_0 d\epsilon_v^p \Rightarrow \frac{\partial \sigma_c}{\partial \epsilon_v^p} = \frac{1 + e_0}{\mathbf{1}(P_c) - k} \sigma_c. \quad (33)$$

Assuming the associated flow rules, the combination of the consistency condition (i.e. $df = 0$ during yield) with the relations (30), (31), (32), and (33) provides the following relations for the plastic strains, in which ξ denotes the ratio between the deviatoric and mean effective stresses ($\xi = \sigma_d/\sigma'_v$):

$$\frac{\partial \epsilon_v^p}{\partial t} = \overset{\circ}{\Lambda} \frac{\partial f}{\partial \sigma'_v}, \quad (34a)$$

$$\frac{\partial \epsilon_d^p}{\partial t} = \overset{\circ}{\Lambda} \frac{\partial f}{\partial \sigma_d}, \quad (34b)$$

where the plastic multiplier is equal to:

$$\overset{\circ}{\Lambda} = \frac{1}{H} \left(\frac{\partial f}{\partial \sigma'_v} \frac{\partial \sigma'_v}{\partial t} + \frac{\partial f}{\partial \sigma_d} \frac{\partial \sigma_d}{\partial t} + \frac{\partial f}{\partial P_c} \frac{\partial P_c}{\partial t} \right), \quad (34c)$$

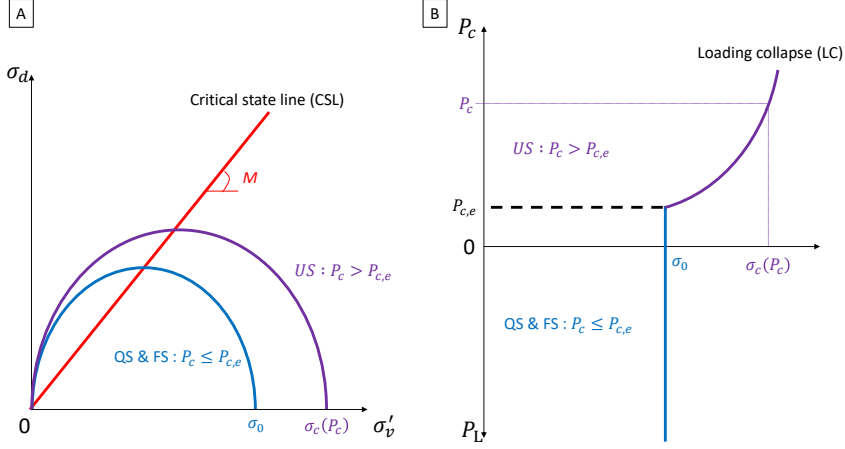


Figure 6: Evolution of the loading surface with suction in the (σ'_v, σ_d) and (σ'_v, P_c) planes.

with

$$H = \frac{(1 + e_0)(\sigma'_v)^3 (M^4 - \xi^4)}{1(P_c) - k} \quad (34d)$$

and

$$\frac{\partial f}{\partial \sigma'_v} = \sigma'_v (M^2 - \xi^2), \quad (34e)$$

$$\frac{\partial f}{\partial \sigma_d} = 2\sigma'_v \xi, \quad (34f)$$

$$\frac{\partial f}{\partial P_c} = (\beta_1 - 1) \frac{(1_{\text{sat}} - k) 1_{\text{sat}}(1 - r) b e^{-b(P_c - P_{c,e})} \ln\left(\frac{\sigma_0}{\sigma_{\text{ref}}}\right)}{(1(P_c) - k)^2} (\sigma'_v)^2 (M^2 - \xi^2). \quad (34g)$$

The combination of (25), (29), and (34) eventually provides:

$$\begin{pmatrix} d\epsilon_v \\ d\epsilon_d \end{pmatrix} = \begin{bmatrix} \frac{1}{K} + \frac{L}{H} \left(\frac{\partial f}{\partial \sigma'_v}\right)^2 & \frac{L}{H} \frac{\partial f}{\partial \sigma'_v} \frac{\partial f}{\partial \sigma_d} & \frac{L}{H} \frac{\partial f}{\partial \sigma'_v} \frac{\partial f}{\partial P_c} \\ \frac{L}{H} \frac{\partial f}{\partial \sigma'_v} & \frac{1}{3G} + \frac{L}{H} \left(\frac{\partial f}{\partial \sigma_d}\right)^2 & \frac{L}{H} \frac{\partial f}{\partial \sigma_d} \frac{\partial f}{\partial P_c} \end{bmatrix} \cdot \begin{pmatrix} d\sigma'_v \\ d\sigma_d \\ dP_c \end{pmatrix}, \quad (35)$$

where $L = 1$ if $f = 0$ (elastoplastic evolution) and $L = 0$ if $f < 0$ (elastic evolution).

4.3. Mechanical equilibrium

If the body forces are neglected, the local mechanical equilibrium leads to the relation:

$$\nabla \cdot \left(\frac{\partial \boldsymbol{\sigma}'}{\partial t} + \frac{\partial \bar{P}_\phi}{\partial t} \boldsymbol{\delta} \right) = \mathbf{0}. \quad (36)$$

The injection of the elastic incremental laws (29) in (36) leads to:

$$\nabla \cdot \left(\mathcal{E}_T : \frac{\partial(\boldsymbol{\epsilon} - \boldsymbol{\epsilon}^p)}{\partial t} + \frac{\partial \bar{P}_\phi}{\partial t} \boldsymbol{\delta} \right) = \nabla \cdot \left(\mathcal{C}_T : \frac{\partial \boldsymbol{\epsilon}}{\partial t} + \frac{\partial \bar{P}_\phi}{\partial t} \boldsymbol{\delta} \right) = \mathbf{0}, \quad (37)$$

where \mathcal{E}_T is the tangent fourth-order tensor of elasticity for which $\mathcal{E}_T : d\boldsymbol{\epsilon}^e = K\epsilon_v^e \boldsymbol{\delta} + 2G\boldsymbol{\epsilon}_d^e$, and $\boldsymbol{\epsilon}$ is related to the displacement field, denoted by \underline{u} through the relation: $\boldsymbol{\epsilon} = -(1/2)({}^t\nabla\underline{u} + \nabla\underline{u})$. Finally, \mathcal{C}_T is the apparent tangent fourth-order elasto-plastic tensor of stiffness.

5. Numerical implementation

5.1. Final set of equations

Within the limits of short-term behaviors for which the diffusion of dissolved air is negligible, the final set of the equation is composed of the two partial differential equations (12-21b) and (37), where the two unknowns are the liquid pressure P_L and the displacement field \underline{u} .

The resulting model uses 12 parameters that can be classified into the following three groups:

- The first group consists of the eight parameters of the elastoplastic rheological law. The elastic parameter \mathbf{k} , the slope of the NCL at saturation ($\mathbf{1}_{\text{sat}}$), and the preconsolidation pressure (σ_0) can be directly determined by conventional isotropic compression tests on saturated soils. They can also be indirectly determined from a saturated oedometer test. The parameters b and r , which express the variation of $\mathbf{1}$ with capillary pressure, can be estimated from two additional isotropic compressions (or oedometer) tests, but under unsaturated conditions. The slope of the CLS (M) and the Poisson coefficient (ν) can be determined from at least one triaxial test (several triaxial tests at several confinement pressures provides a better assessment). Finally, the initial void ratio e_0 can be estimated from the mass variation between fully saturated and dried states.
- The second group contains the three parameters of the retention curve: $P_{c,e}$, a , and S_e .
- The last group contains the two transport parameters, namely \mathcal{K}_L and δ_p , which can be determined from classical standardized tests. If the long-term behavior is considered, the knowledge of an additional parameter, namely the effective diffusion of dissolved air (D_e^v), is required.

5.2. Discretisation

The following developments will be limited to 1D problems under oedometric conditions along the x axis. In that case, all quantities only depend on the spatial coordinate x and time t while $\underline{u} = u\mathbf{e}_x$ and thus $\epsilon_{xx} = -\partial u/\partial x$ is the sole non null component of $\boldsymbol{\epsilon}$. For the stress field, only σ_{xx} intervenes in the unique equilibrium condition $\partial\sigma_{xx}/\partial x = 0$. The external surface force $\underline{T} = -\boldsymbol{\sigma} \cdot \underline{n}$, with \underline{n} the outgoing normal vector, is the external surface force, also reduces to a scalar T (the x -component) at each of the two extremities.

The multiplication of the two equations respectively by a virtual displacement field, denoted by $\underline{u}^* = u^*\mathbf{e}_x$, and a virtual pressure field P^* followed by an integration leads, after simplification and while neglecting the variation S_{aG}^m with e , to the following expression for the variational formulation:

$$\int_{\Omega} \left(\boldsymbol{\epsilon}(u^*) : \mathcal{C}_T : \boldsymbol{\epsilon}(\dot{u}) - \frac{\partial u^*}{\partial x} \frac{\partial \bar{P}_{\phi}}{\partial t} \right) d\Omega = \int_{\Gamma} u^* \frac{\partial T}{\partial t} d\Gamma, \quad (38)$$

$$\int_{\Omega} \left(\phi \rho_L^0 P^* \left(A_p \frac{\partial P_L}{\partial t} - \frac{\partial S_{\text{aG}}^{(t)}}{\partial t} + \frac{S_L}{\phi} \frac{\partial \dot{u}}{\partial x} \right) + \frac{\partial P^*}{\partial x} D_L \frac{\partial P_L}{\partial x} \right) d\Omega = \int_{\Gamma} P^* q_L d\Gamma, \quad (39)$$

where Ω is the total volume of the domain and Γ is its surface. The notations $\phi = e/(1 + e_0)$ and $\dot{u} = \partial u/\partial t$ are used to simplify the reading of expressions, while $q_L = D_L \nabla P_L \cdot \underline{n}$ is the water influx at the external surface.

Using the classic finite element discretization, the integral over the domain Ω is the sum of integrals over each element Ω_i . The displacements and pressure fields inside an element at any time t is expressed as a combination of the elementary nodal displacements via a set of shape functions:

$$u(x, t) = \sum_k N_{i,j}^u U_{i,j}; \quad u^*(x, t) = \sum_k N_{i,j}^u U_{i,j}^*, \quad (40)$$

$$P_L(x, t) = \sum_k N_{i,k}^p P_{i,j}; \quad P^*(x, t) = \sum_k N_{i,k}^p P_{i,k}^*. \quad (41)$$

The choice of the type of element for the spacial discretization is essential. As noted by [30], the interpolation degree for the displacement fields must be strictly higher than those of pressure fields. Here, the same approach as the one developed in [15] is used, which consists in considering linear elements for pressure fields ($k = 2$) and quadratic elements for displacement fields ($j = 3$). It leads to the spacial discretization represented in the Figure 7.

Applying the above discretization to the variational equations, and after assembling the elementary contributions, while accounting for the arbitrariness of the virtual field, we get:

$$\mathcal{D} \frac{\partial \mathbf{U}}{\partial t} + \mathcal{Q} \frac{\partial \mathbf{P}}{\partial t} = \mathbf{F}_S^u + \mathbf{F}_T^u, \quad (42)$$

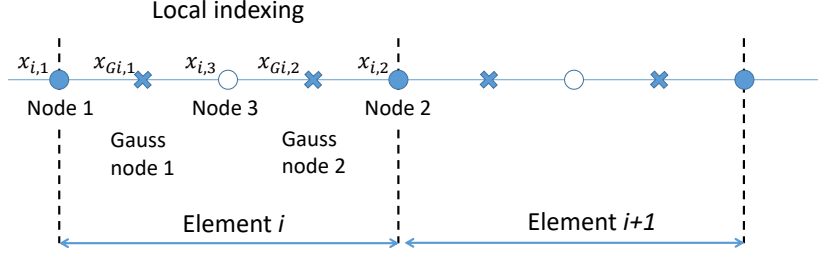


Figure 7: Diagram of an element i with 3 interpolation node for the displacement (nodes 1, 2 and 3), two nodes for the pressure (nodes 1 and 2) and two Gauss nodes.

$$\mathcal{R} \frac{\partial \mathbf{U}}{\partial t} + \mathcal{S} \frac{\partial \mathbf{P}}{\partial t} + \mathcal{T} \mathbf{P} = \mathbf{F}_S^p + \mathbf{F}_q^p \quad (43)$$

where \mathbf{U} and \mathbf{P} are the global matrices of nodal displacements and pressure at the structural level, with \mathcal{D} , \mathcal{Q} , \mathcal{R} , \mathcal{S} , \mathcal{T} , \mathbf{F}_S^u , \mathbf{F}_T^u , \mathbf{F}_S^p and \mathbf{F}_q^p coming from the assemblage of elementary matrices \mathcal{D}_i , \mathcal{Q}_i , \mathcal{R}_i , \mathcal{S}_i , \mathcal{T}_i , $\mathbf{F}_{S,i}^u$, $\mathbf{F}_{T,i}^u$, $\mathbf{F}_{S,i}^p$ and $\mathbf{F}_{q,i}^p$ of the form:

$$\begin{aligned} \mathcal{D}_i &= \int_{\Omega_i} (\mathbf{B}_i^u)^t \mathcal{C}_T \mathbf{B}_i^u d\Omega ; \\ \mathcal{Q}_i &= - \int_{\Omega_i} (\mathbf{B}_i^u)^t ((1 - \beta_1)(1 - a)S_L + \beta_1) \mathbf{N}_i^p d\Omega ; \\ \mathbf{F}_{S,i}^u &= \int_{\Omega_i} (\mathbf{B}_i^u)^t \beta_1 P_{c,e} \frac{\partial S_{aG}^{(t)}}{\partial t} d\Omega ; \\ \mathbf{F}_{T,i}^u &= \int_{\Omega_i} (\mathbf{N}_i^u)^t \frac{\partial T}{\partial t} d\Omega ; \\ \mathcal{R}_i &= \int_{\Omega_i} (\mathbf{N}_i^p)^t \rho_L^0 S_L \mathbf{B}_i^u d\Omega ; \\ \mathcal{S}_i &= \int_{\Omega_i} (\mathbf{N}_i^p)^t \phi \rho_L^0 A_p \mathbf{N}_i^p d\Omega ; \\ \mathcal{T}_i &= \int_{\Omega_i} (\mathbf{B}_i^p)^t D_L \mathbf{B}_i^p d\Omega ; \\ \mathbf{F}_{S,i}^p &= \int_{\Omega_i} (\mathbf{N}_i^p)^t \phi \rho_L^0 \frac{\partial S_{aG}^{(t)}}{\partial t} d\Omega ; \\ \mathbf{F}_{q,i}^p &= \int_{\Omega_i} (\mathbf{N}_i^p)^t q_L d\Omega ; \end{aligned}$$

where

$$\mathbf{N}_i^u = [N_{i,1}^u \ N_{i,2}^u \ N_{i,3}^u] ; \mathbf{N}_i^p = [N_{i,1}^p \ N_{i,2}^p] ; \mathbf{B}_i^u = \frac{\partial N_i^u}{\partial x} ; \mathbf{B}_i^p = \frac{\partial N_i^p}{\partial x}.$$

5.3. Resolution scheme

This poro-elastoplastic system of equations was implemented in the code Hydromec1D initially developed by [15]. The resolution uses a classical iterative method to compute the stress correction due to the plastic strain, based on the elastic stiffness. For this 1D problem, where computation time is not an issue, a very small time step is used to ensure convergence.

6. Results and discussion

The consistency of the results provided by the model was tested on a comparison with the experimental data provided by Magnan and Dang [31], which is illustrated in Figure 8. This experiment is described in detail in [32].

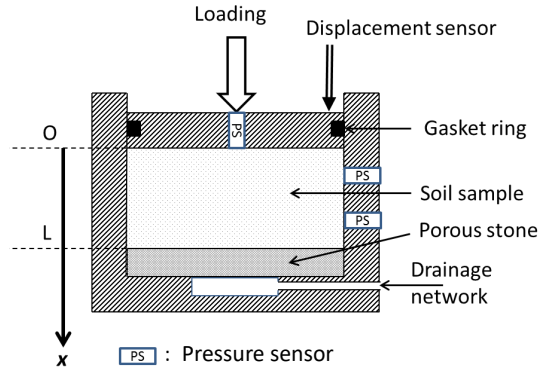


Figure 8: Diagram of the consolidated-undrained oedometer test on clay samples from Cubzacles-Ponts conducted by [31].

Roughly it consists in an undrained oedometer test, with an axial stress ranging from 28 kPa to 800 kPa, on a quasi-saturated 5-cm-high sample 6.5 cm in diameter. To simulate this test, the system of equation (12-21b) and (37) is solved using an adaptation of the finite element code *Hydromech* developed by [15]. In this experiment, the soil sample was taken from a site in Cubzacles-Ponts, in southeastern France, whose parameters are summarized in Table 2 (data provided by [33]).

Two simulations were performed: with and without air dissolution. The results are reported in Figure 9.

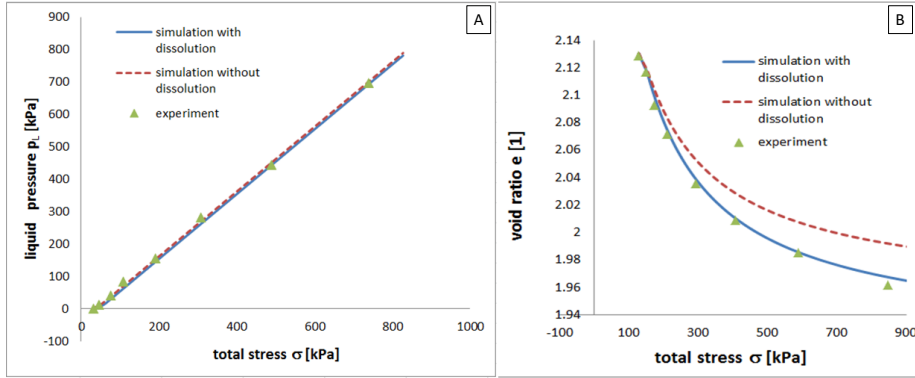


Figure 9: Comparison between the model results and the data from Magnan and Dang’s experiment

A good match is observed between the calculated excess pore pressures and those from the experimental measurements (cf. Figure 9A). Moreover, it can be observed that the consideration of air dissolution significantly affects the model’s prediction. For this example, and with the set of material parameters adopted, the simulation that takes into account air dissolution leads to a better estimation of the void ratio evolution, whereas the simulation ignoring air dissolution underestimates the deformability (see Figure 9B). The difference between the two simulations is significant because the soil under consideration is highly deformable. These results highlight the importance to take into account the air dissolution phenomenon for a precise estimation of the deformability of quasi-saturated soils.

Symbol	Description	Value [unity]
e_0	Initial void ratio	2.13
k	Slope of the swelling line	0.05
ν	Poisson’s ratio	0.3
l_{sat}	Slope of the NCL at saturation	0.6
b	Model parameter	0.75
r	Model parameter	$12.5 \text{ [MPa}^{-1}\text{]}$
σ_0	Preconsolidation pressure at saturation	28 [kPa]
M	Slope of the CLS	0.75
S_e	Degree of saturation at air entry	0.915
$P_{c,e}$	Entry air suction	110 [kPa]
a	Coefficient of the retention curve	0.4
\mathcal{K}_L^0	Coefficient of permeability at saturation	$5 \times 10^{-10} \text{ [s]}$
δ_p^0	Dried effective diffusion of vapor	$1.5 \times 10^{-11} \text{ [s]}$

Table 2: Material parameter of the soil from Cubzac-les-Ponts from [33].

The same kind of results were obtained using an elastic approach in [14]. However, contrary to what it was made in [14], where it was necessary to adjust the value of the elastic parameters, the elasto-plastic parameters used to obtain the results of the Figure 9 were directly the ones provided by [33]. In other words, no calibration of model parameter was realized.

This result gives thus some confidence on the accuracy of this model when the soil remains in the quasi-saturated domain. It is however not sufficient to test the model's ability to correctly reproduce the transitions (both spacial and temporal) among the several domains of saturation and to analyze the importance of taking into account the elasto-plastic processes.

For this purpose, a theoretical simulation was undertaken considering an oedometric imbibition (null radial displacement and flows) at constant axial stress. An initially unsaturated homogeneous 5-cm-thick sample was subjected to a monotonic increase of liquid pressure at the top boundary surface ($x = 0$), from -250 [kPa] to 900 [kPa] in 150[s]. At the bottom boundary ($x = 5\text{cm}$), a no-flux condition was considered. The total axial stress was kept constant equal to its initial value $\sigma_{xx}(x, t) = 1\text{MPa}$. Finally, the mass concentration of dissolved air in the incoming liquid water was, at any time, equal to the concentration of dissolved air within the pores of the sample, which were directly in contact with the external surfaces. The results of this simulation are shown in Figure 10.

Until $t = 37\text{s}$ the whole sample is unsaturated (US). The liquid saturation profile is directly linked to the liquid pressure through the retention curve (8) because the gas pressure is kept equal to P_{atm} . At $x = 0\text{m}$, the transition between the unsaturated (US) and quasi-saturated (QS) domains occurs for $t = 37\text{s}$. This is illustrated by the variation in shape of both $S_L(t)$ (see Figure 10A) and $P_G(t)$ curves (see Figure 10B). The former stems from the modification of the link between S_L and P_L , which is no longer driven by (8) in the quasi-saturated domain, but by air dissolution and compressibility, as depicted by the relation (21b). The latter is the consequence of the assumptions that the gas pressure is equal to the atmospheric pressure in the unsaturated domain and that the difference between the gas pressure and the liquid pressure becomes constant in the quasi-saturated domain (see eq. (10)). In line with (26), this augmentation of the gas pressure induces a reduction of the effective stress. It explains the increase of slope observed in Figure 10D, which denotes an acceleration of the void ratio increase when the material becomes quasi-saturated. In addition, as it is shown in Figures 10C and D, the decrease in effective stress induces an elastoplastic transition, which occurs while the material is under the quasi-saturated regime of saturation. In consequence, an accurate modeling of the quasi-saturated domain appears to be important for an accurate prediction of the soil deformation.

At $x = 0\text{m}$ and $t = 145\text{s}$, the value of the saturation ratio reaches 1, and the material becomes fully saturated. From then on, the saturation remains

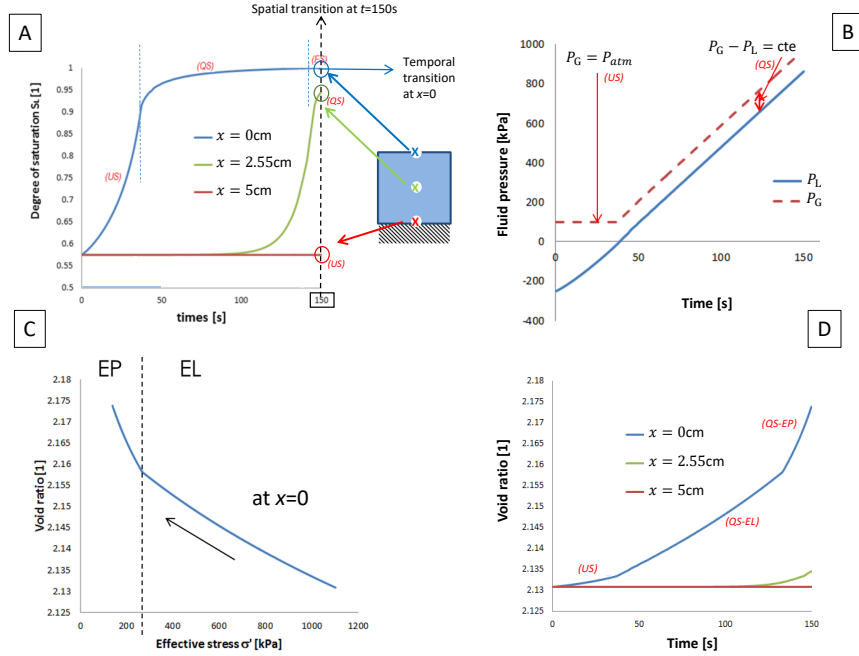


Figure 10: Results of the numerical simulation of oedometric imbibition. US, QS, and FS stand for the unsaturated, quasi-saturated, and fully saturated domains, respectively. A: Saturation ratio at three locations over time. B: Evolution at $x = 0$ of liquid and gas pressures. C: Effective stress at the $x = 0$ surface over time. D: Evolution of the void ratio as a function of the effective stress at $x = 0$. The dotted line represents the transition between the elastic (EL) and the elastoplastic (EP) behaviors. E: Void ratio at three locations over time.

constantly equal to 1. This analysis demonstrates the ability of the model to reproduce temporal transitions of saturation domains, irrespective of the mechanical behavior of the solid skeleton (either elastic or elastoplastic).

Finally, the ability of the model to reproduce the spacial transitions of saturation domains is illustrated in Figure 10A, in which a coexistence of the three saturation domains can be observed at $t = 150$ s.

These two numerical examples demonstrate some of the abilities of the theoretical framework developed. However, the extent to which this degree of complexity is necessary to properly design earthworks near saturation can be questioned. Concerning the entrapped air dissolution process, the first numerical example shows the strong effects on both soil deformability and the evolution of entrapped air content with in-pore pressure. Ignoring this phenomenon would underestimate the deformability of the soil and to overestimate the air content within the soil. It would thus be prejudicial in the assessment of rutting, for example.

A great asset of this model is that it allows continuous and smooth spatial and temporal transitions between the saturation domains. The importance of the transition between the unsaturated and the quasi-saturated states is quite obvious. Although the top layer of an earthwork (such as an earth dam or a road or railway embankment) is quite often in an unsaturated state, the deeper layers remain quasi-saturated. Thus, interfaces between the saturation domains will be present, and a simulation that considers only one saturation domain will not accurately estimate the global deformation of the earthwork. In addition, using physical parameters of real soil, the model predicts a transition between the quasi-saturated and the fully saturated domains for an excess pore water pressure of 300 kPa, which corresponds to a 30-m column of water. In all cases in which such excess pore pressures may be encountered, the transitions between the saturation domains should be taken into account.

Other models allowing one to take into account the entrapped air phase and to consider transitions of the saturation domain have already been developed in the past. Compared to these models, the main addition of this new model is to provide a better physical description of the behavior of entrapped air by considering that it is attached to the solid skeleton rather than to the fluid phase and that its pressure is driven by the liquid-gas interface curvature, which tends to be as small as possible. However, without additional experimental data, no definitive conclusion can be drawn on the most accurate strategy to model quasi-saturated soils.

In addition, this model is still subjected to some major limitations. At first, only isothermal configurations are considered. As it is underlined by [34, 35], temperature variations would affect the elasto-plastic behavior of the soil, its retention curve (similarly to what is presented in [36]) and dissolution/bubbling processes of entrapped air. Thus, spatial and temporal variations of the temperature field may significantly change the impact of the entrapped air on the global behavior of the soil. Secondly, this model assumes that the material is isotropic, which is unlikely due to the directional compaction method commonly used. A more realistic model would therefore assume a transverse isotropic behavior such as the one depicted by [37] for Tournemire argillites. Among the same line, if clay soils are considered, it might not be entirely justified to assume that the compressibility of the solid matrix is negligible. It would be necessary to introduce the Biot's coefficient in the expression of the effective stress and to consider the variation of porosity at constant macroscopic strain caused by the deformation of solid particles [20]. Finally, for a global hydromechanical assessment, the impact of the pore space deformations (plastic, thermal, cracks, etc.) on the transfer properties, which may be far from negligible [38], as well as the hysteresis of the retention curve in the US domain [39] should be taken into account.

7. Conclusion

The behaviour of quasi-saturated materials is an important factor to be considered when designing cuttings and embankments in which earthwork materials are compacted to the optimum proctor density. Typically, soil compaction is performed at the optimum Proctor or on the wet side of the optimum, which means that the soil is in a highly saturated state. In such case, the gas phase may become discontinuous and take the form of entrapped air pockets. In this context, the construction of a theoretical model for this type of soils was presented in this paper. It has required the consideration of various physical-mechanical phenomena and their couplings occurring within the tri-phasic medium consisting of the solid grains, liquid water containing dissolved air and the entrapped air pockets. In particular, the conditions leading to the presence of these pockets within the porous network, their evolution and their migration were discussed. Although they are trapped in the pores, their dissolution can take place. Dissolved air can migrate through the pore space, either by following the flow of the fluid or by diffusion. The development leads to a system of highly non-linear partial differential equations which was solved numerically using the finite element method. A simplification of the system for short term behaviors was then proposed.

On the basis of this simplified system, a new elasto-plastic hydromechanical model has been developed that takes into account the physical-mechanical interactions between these different in-pore phases and the solid matrix. For that purpose, a bishop effective stress with $\xi(S_L) = S_L$ was considered, and no variation of preconsolidation effective stress and of the slope of the NCL were assumed when the soil is quasi-saturated.

This new model has been implemented in a numerical code Hydromech written in C++, developed originally by [15] that has been used to simulate oedometer tests with different hydromechanical loading paths. In particular, this code allows to simulate consistently the transition across different regimes of saturation, both with respect to space (progressive translation of a boundary between two neighbouring regimes) and to time (transition of one regime to another at a fixed material point); which constituted a difficult modelling problem at the start. Numerical studies carried out show that this model gives consistent results providing a clear demonstration of its ability to simulate with precision the hydro-mechanical behaviour of quasi-saturated soils containing entrapped air.

References

- [1] C. Gallage, J. Kodikara, and T. Uchimura. Laboratory measurement of hydraulic conductivity functions of two unsaturated sandy soils during drying and wetting processes. *Soils and Foundations*, 53:417–430, 2013.
- [2] B. Francois, S. Salager, M.S. El Youssoufi, D. Ubals Picanyol, L. Laloui, and C. Saix. Compression tests on a sandy silt at different suction and

- temperature levels. *ASCE Geotechnical Special Publication: Computer Applications in Geotechnical Engineering*, 157, 2007.
- [3] D.Y.F Ho, D.G. Fredlund, and H. Rahardjo. Volume change indices during loading and unloading of an unsaturated soil. *Canadian Geotechnical Journal*, 29:195–207, 1992.
- [4] J.M Fleureau, S. Kheirbek-Saoud, R. Soemitro, and S. Taibi. Behavior of clayey soils on drying?wetting paths. *Canadian Geotechnical Journal*, 20:293–296, 1993.
- [5] E.E. Alonso, A. Gens, and A. Josa. A constitutive model for partially saturated soils. *Géotechnique*, 40:405–30, 1990.
- [6] DG. Fredlund. The 1999 r.m. hardy lecture: the implementation of unsaturated soil mechanics into geotechnical engineering. *Canadian Geotechnical Journal*, 37:963–86, 2000.
- [7] M. Nuth and L. Laloui. Effective stress concept in unsaturated soils: clarification and validation of unified framework. *International Journal for Numerical and Analytical Methods in Geomechanics*, 32:771–801, 2008.
- [8] D. Sheng. Review of fundamental principles in modelling unsaturated soil behaviour. *Computer and Geotechnics*, 38:757–776, 2011.
- [9] A-N. Zhou and D. Sheng. An advanced hydro-mechanical constitutive model for unsaturated soils with different initial densities. *Computers and Geotechnics*, 63:46–66, 2015.
- [10] J. Christiansen. Effect of entrapped air upon the permeability of soils. *Soil Science*, 58:355–65, 1944.
- [11] D. A. Stonestrom and J. Rubin. Water content dependence of trapped air in two soils. *Water resources research*, 25:1947–1958, 1989.
- [12] B. Faybishenko. Hydraulic behavior of quasi-saturated soils in the presence of entrapped air: laboratory experiments. *Water Resource Research*, 31:2421–2435, 1995.
- [13] L. Boutonnier. *Comportement hydromécanique des sols fins proches de saturation cas des ouvrages en terre: coefficient B, déformations instantanées et différées, retrait/gonflement*. PhD thesis, Institut National Polytechnique de Grenoble, 2007.
- [14] B.T. Lai, A. Fabbri, H. Wong, and D. Branque. Poroelastic behaviour of fine compacted soils in the unsaturated to saturated transition zone. *Computers and Geotechnics*, 69:627–640, 2015.
- [15] J.M. Pereira. *Etude des couplages hydromécaniques et effets de non saturation dans les géomatériaux. Application aux ouvrages souterrains*. PhD thesis, Ecole Nationale des Travaux Publics de l’Etat, 2005.

- [16] P. Vaughan. Observations on the behaviour of clay fill containing occluded air bubbles. *Geotechnique*, 53:265–72, 2003.
- [17] E. Schuurman. The compressibility of an air/water mixture and theoretical relation between the air and water pressures. *Geotechnique*, 16(4):269–281, 1966.
- [18] B. Faybishenko. Influence of entrapped on soils permeability: theory and experiment. *Vodn Resur*, 4:48–60, 1984.
- [19] Y. Higo, R. Morishita, R. Kido, G. Khaddour, and S. Salager. Local water-retention behaviour of sand during drying and wetting process observed by micro x-ray tomography with trinarisation. *Japanese Geotechnical Society Special Publication*, pages 365–368, 2015.
- [20] O. Coussy. *Mechanics and Physics of Porous Solids*. Wiley, 2010.
- [21] F. Osselin, A. Fabbri, T. Fen-Chong, J.M. Pereira, A. Lassin, and P. Dangla. Poromechanics of salt nucleation within a unsaturated reservoir rock. *5th Biot Conference on Poromechanics*, 2013.
- [22] R.H. Brooks and A.T. Corey. Hydraulic properties of porous media and their relation to drainage design. *Transactions of the ASAE*, 7:26–28, 1964.
- [23] S.K. Vanapalli, D. Fredlund, and D.E. Pufahl. The influence of soil structure and stress history on the soil-water characteristics of a compacted till. *Geotechnique*, 49:143–159, 1999.
- [24] Z. Cabarkapa and T. Cuccovillo. Automated triaxial apparatus for testing unsaturated soils. *Geotechnical Testing Journal*, 29:1–9, 2006.
- [25] P.L. Martin, E.E. Alonso, and J. Alcoverro. Bm 3.2: Febex mock-up test. benchmark definition. *Report of the Catsius clay project*, 1998.
- [26] R.J. Millington. Gas diffusion in porous media. *Science*, 130:100–102, 1959.
- [27] O. Coussy, P.M. Pereira, and J. Vaunat. Revisiting the thermodynamics of hardening plasticity for unsaturated soils. *Computers and Geotechnics*, 37:207–215, 2010.
- [28] P.T. Cruz. Peculiarities of tropical lateritic and saprolitic soils used as construction materials, selection, control and acceptance criteria-dams. *Progress report of committee on tropical and saprolitic soils, Brazilian society of soil mechanics*, pages 275–327, 1985.
- [29] J.T. Shahu, Yudhbir, and N.S.V. Kameswara Rao. Effective stress behavior of quasi-saturated compacted cohesive soils. *ournal of Geotechnical and Geoenvironmental Engineering*, 124:125–144, 1962.

- [30] O.C. Zienkiewicz and R.L. Taylor. *The Finite Element Method. Fifth edition. Volume 2: Solid Mechanics*. Butterworth Heinemann, 1999.
- [31] J.P. Magnan and M.T. Dang. Etude théorique et expérimentale de la compressibilité du fluide interstitiel dans un sol argileux presque saturé. Technical report, LCPC, 1977.
- [32] B.T. Lai, H. Wong, A. Fabbri, and D. Branque. A new constitutive model of unsaturated soils using bounding surface plasticity (bsp) and a non-associative flow rule. *Innov. Infrastruct. Solut.*, 1:3, 2016.
- [33] J. Monnet and L. Boutonnier. Calibration of an unsaturated air-water-soil model. *Archives of civil and mechanical engineering*, pages 493–499, 2012.
- [34] B. Francois and L. Laloui. ACMEG-TS: A constitutive model for unsaturated soils under non-isothermal conditions. *International Journal for Numerical and Analytical Methods in Geomechanics*, 32:1955–1988, 2008.
- [35] Y.P. Yao and A.N. Zhou. Non-isothermal unified hardening model: a thermo-elasto-plastic model for clays. *Géotechnique*, 63:1328–1345, 2013.
- [36] A. Fabbri, F. McGregor, I. Costa, and P. Faria. Effect of temperature on the sorption curves of earthen materials. *Materials and Structures*, 50:253, 2017.
- [37] A. Noiret, R. Giot, E. Bemer, A. Giraud, and F. Homand. Hydromechanical behavior of tournemire argillites: Measurement of the poroelastic parameters and estimation of the intrinsic permeability by oedometric tests. *International Journal for Numerical and Analytical Methods in Geomechanics*, 35:496–518, 2011.
- [38] M. Monfared, J. Sulem, P. Delage, and M. Mohajerani. Temperature and damage impact on the permeability of opalinus clay. *Rock Mechanics and Rock Engineering*, 47:101–110, 2014.
- [39] A-N. Zhou. A contact angle-dependent hysteresis model for soil-water retention behaviour. *Computers and Geotechnics*, 49:36–42, 2013.